Colloids and Surfaces B: Biointerfaces 145 (2016) 382–391

Contents lists available at ScienceDirect

Colloids and Surfaces B: Biointerfaces

journal homepage: www.elsevier.com/locate/colsurfb

# Biomimetic fiber mesh scaffolds based on gelatin and hydroxyapatite nano-rods: Designing intrinsic skills to attain bone reparation abilities

Javier Sartuqui[a], A. Noel Gravina[a], Ramón Rial[b], Luciano A. Benedini[a], L'Hocine Yahia[c], Juan M. Ruso[b], Paula V. Messina[a,*]

[a] Department of Chemistry,Universidad Nacional del Sur, INQUISUR – CONICET, 8000 Bahía Blanca, Argentina
[b] Soft Matter and Molecular Biophysics Group, Department of Applied Physics, University of Santiago de Compostela, Santiago de Compostela E-15782, Spain
[c] Laboratory for Innovation and Analysis of Bio-Performance, École Polytechnique de Montréal, C.P. 5079, Succursale Centre-Ville Montréal, Quebec H3C 3A7, Canada

ARTICLE INFO

*Article history:*
Received 6 April 2016
Received in revised form 29 April 2016
Accepted 5 May 2016
Available online 9 May 2016

*Keywords:*
Gelatin
Tannic acid
Hydroxyapatite
Tissue engineering
Macroporosity
Scaffolds

ABSTRACT

Intrinsic material skills have a deep effect on the mechanical and biological performance of bone substitutes, as well as on its associated biodegradation properties. In this work we have manipulated the preparation of collagenous derived fiber mesh frameworks to display a specific composition, morphology, open macroporosity, surface roughness and permeability characteristics. Next, the effect of the induced physicochemical attributes on the scaffold's mechanical behavior, bone bonding potential and biodegradability were evaluated. It was found that the scaffold microstructure, their inherent surface roughness, and the compression strength of the gelatin scaffolds can be modulated by the effect of the cross-linking agent and, essentially, by mimicking the nano-scale size of hydroxyapatite in natural bone. A clear effect of bioactive hydroxyapatite nano-rods on the scaffolds skills can be appreciated and it is greater than the effect of the cross-linking agent, offering a huge perspective for the upcoming progress of bone implant technology.



## 1. Introduction

The physical and biological requests of an ideal synthetic bone substitute involve frameworks that closely mimic human tissue morphology, but also that are optimized to perform host tissue's specific functions [1]. The human skeleton has an obvious mechanical function in supporting and protecting the body [2]. Therefore, it becomes critically important to design scaffolds that must maintain their physical integrity during applications subjected to mechanical stresses, which might lead to bearing superior body loads [3]. In a previous work [4], we have evaluated the hydrodynamic and crowding evolution of aqueous gelatin/hydroxyapatite nano-rods systems with the aim of increasing the knowledge about the collagen mineralization biomimesis, and how it can be manipulated for the preparation of collagenous derived frameworks with specific morphological characteristics. Gelatin is a partially degraded product of collagen; compared to its precursor has lower cost, it is low-antigenic, and retains specific collagen information signals, such as the Arginyl-glycyl-aspartic acid (RGD) tri-peptide, which can partially enhance the cell-adhesive activity [5,6]. Recently, gelatin-based biomaterials have been applied to artificial skin, [7] bone grafts, [8] and scaffolds for tissue engineering [9,10]. In this study, we have prepared improved gelatin-hydroxyapatite (HA) nano-composites using a natural phenolic compound, tannic acid (TA), as a cross-linking agent to reduce the solubility of gelatin in aqueous environments at the human-body temperature [5]. TA exhibits antioxidant activity, in addition of recently reported anti-allergenic, anti-inflammatory, anti-microbial, cardio-protective and anti-thrombotic properties [11] making this compound a very interesting raw material for the development of novel medical applications. Bio-mineralization, compression, bone bonding potential and degradation tests were carried out to determine the potential use of gelatin-HA scaffolds on calcified tissue reparation. It was found that the microstructure and the compression strength of the gelatin scaffolds can be modulated by the effect of the crosslinking agent and, particularly, by mimicking the nano-size scale of HA in natural bone. The presence of pre-embedded HA nanoparticles on gelatin scaffolds has a clear effect on the epitaxial growth of the mineralized phase deposition denoting their potential role in the process of

* Corresponding author.
*E-mail address:* pmessina@uns.edu.ar (P.V. Messina).

http://dx.doi.org/10.1016/j.colsurfb.2016.05.019
0927-7765/

bio-mineralization and, subsequently in the scaffolds' mechanical behavior, bone bonding potential and biodegradability properties.

## 2. Materials and methods

### 2.1. Reagents

Hexadecyl-trimethyl ammonium bromide (CTAB, MW = 364.48 g mol$^{-1}$, 99% Sigma-Aldrich), poly (propylene glycol) (PPG, Sigma-Aldrich, MW = 425 g mol$^{-1}$, δ = 1.004 g cm$^{-3}$ at 25 °C), sodium phosphate ($Na_3PO_4$, MW = 148 g mol$^{-1}$, 96% Sigma-Aldrich), calcium chloride ($CaCl_2$, MW = 91 g mol$^{-1}$, 99% Sigma-Aldrich), sodium nitrite ($NaNO_2$, MW = 69 g mol$^{-1}$, 97% Sigma-Aldrich), acetic acid ($C_2H_4O_2$, MW = 60.05 g mol$^{-1}$, 99% Sigma-Aldrich), sodium acetate tri-hydrate ($C_2H_3NaO_2{\cdot}3H_2O$, MW = 136.03 g mol$^{-1}$, 99% Sigma-Aldrich), sodium hydroxide (NaOH, MW = 40 g mol$^{-1}$, 90% Sigma-Aldrich), commercial gelatin (GE) from bovine skin (Grade OR, Type B, 225 Bloom, MW ≈ 50000 g mol$^{-1}$, Merck), tannic acid ($C_{76}H_{52}O_{46}$, MW = 1701.20 g mol$^{-1}$, 99% Sigma-Aldrich), tris(hydroxymethyl)aminomethane hydrochloride (Tris-HCl, 99% Sigma-Aldrich), phosphate buffer saline (PBS tablets, Sigma-Aldrich) and lysozyme from chicken egg (LSZ for molecular biology, Sigma-Aldrich) were used without further purification. For solutions preparation, only triplet-distilled water was used.

### 2.2. Preparation of fibrous gelatin-nano-HA scaffolds

Bone-like HA nanoparticles of 8 ± 1 nm diameters and 28 ± 3 nm length were made by a previously described methodology [12], for details see supplementary material (SM). To obtain the cross-linked gelatin-HA scaffolds, a 0.80 g/mL GE solution was prepared by dissolution of the proper amount of commercial GE in 35 mL of sodium acetate buffer (pH = 4.5). First, GE was left to hydrate for 30 min at RT, and then dissolved at 58 °C under stirring at 500 rpm during 30 min; finally it was allowed to rest in a thermostatic bath for 24 h in order to reach equilibrium. Afterward 0.85 mg/mL of HA nanoparticles were added to the previously described GE solution under vigorous sonication. After the homogeneous dispersion of HA into GE solution was obtained, cross-linking modified scaffolds were prepared using TA as cross-linking agent. First, GE-HA solution's pH was adjusted to pH = 11 by addition of $NaHCO_3$. Second, TA powder (12.4 and 33.3 mg/g GE) was added to the solution slowly under stirring at 500 rpm. Finally, after the integration of all reagents, the solution was magnetically stirred for 20 min to achieve the crosslinking process. The obtained gels were cooled under −50 °C during 24 h and lyophilized in a Rificor L-A-B4 lyophilizer. The selected amounts of GE, TA and HA used in this work are the suitable to guarantee an effective cross-linking effect on the gelatin matrix avoiding the grafting and branching reactions in conjunction with the hydrogen bonding between gelatin and TA molecules [13]; and for the attainment of an uniaxial orientation porous framework [4]. A summary of the reagent quantities was shown in supplementary material (Table SM1). Scaffolds mineralization process was performed following the layer by layer deposition method described by Taguchi et al. [14], see details in SM.

### 2.3. Structural characterization of cross-linked gelatin-HA scaffolds

#### 2.3.1. Field emission scanning electron microscopy (FE-SEM)

Surface morphology was evaluated using a field emission scanning electron microscope (ZEISS FE-SEM ULTRA PLUS). To acquire all the SEM images a secondary electron detector was used. The accelerating voltage (EHT) applied was 3.00 kV with a resolution (WD) of 2.1 nm. Local compensation of charge (by injecting nitrogen gas) was applied avoiding the sample staining. The associated energy-dispersive spectrophotometer provided qualitative information about surface elemental composition. The pore sizes of scaffolds (determined from about 100 measurements) and the topography (calculating the Skewness ($R_{sw}$) and Kurtosis ($R_{ku}$)) of samples were quantified from SEM microphotographs using an image visualization software (Image J 1.34 s, NIH Image, USA) [15] with an uncertainty of 5%. For details, see SM.

#### 2.3.2. High resolution transmission electron microscopy (H-TEM)

H-TEM microphotographs were taken using a Libra 200 FE OMEGA transmission electron microscope operated at 200 kV with magnification of 1,000,000×. Observations were made in a bright field. Powdered samples were placed on carbon supports of 2000 mesh. The equipment is provided with electron diffraction (ED) system; d-spacing is computed based on the Bragg Law derived equation ($rd = L\lambda$), where "$r$" is the spot distance in the ED pattern, and $L\lambda = 1$ is the camera constant.

#### 2.3.3. X-ray powder diffraction

Powder X-ray diffraction (XRD) data were collected with a Philips PW 1710 diffractometer with Cu Kα radiation (λ = 1.5418 nm) and graphite monochromator operated at 45 kV; 30 mA and 25 °C.

#### 2.3.4. FT-IR spectroscopy

The experiments were done in a VARIAN FT-IR 670 spectrophotometer. To avoid co-adsorbed water, the samples were dried under vacuum until constant weight was attained and diluted with KBr powder before the FT-IR spectra were recorded.

### 2.4. Open porosity

The open porosity of the synthesized scaffolds was measured based on Archimedes's principle using a specific gravity bottle. We optimized this methodology by testing various immersion liquids as well as by establishing a standard test procedure following the Active Standard ASTM B962. Briefly, the open porosity of cubic shaped (≈ 0.71 cm edge) scaffold's samples was determined as follows: [16]

$$Porosity\,(\%) = \frac{(W_2 - W_3 - W_s)/\rho_e}{(W_1 - W_3)/\rho_e} \quad (1)$$

where, $W_1$ is the specific gravity bottle weight filled with ethanol, $W_2$ is the specific gravity bottle weight including ethanol and scaffold section, $W_3$ is the specific gravity bottle weight measured after taking out ethanol-saturated scaffold section from $W_2$, $W_s$ is the ethanol-saturated scaffold section weight and $\rho_e$ the density of ethanol; thus $(W_1 - W_3)/\rho_e$ is the total volume of the scaffold including pores and $(W_2 - W_3 - W_s)/\rho_e$ is the pore volume in the scaffold.

### 2.5. Swelling kinetics and solvent absorption capacity

Swelling kinetics of the samples were carried out following a conventional gravimetric procedure. [16] Vacuum-dried cubic scaffolds samples (0.71 cm edge) were weighed before and after soaking in 0.1 M PBS kept in a thermostatic water bath at 37 °C. Samples were taken out after regular intervals of time and weighted. Weight of all gels was taken until the equilibrium was reached. Each experiment was repeated three times. The water uptake capacity ($\%W_u$) is given by: [16]

$$\%W_u = \frac{(W_t - W_d)}{W_e} \times 100 \quad (2)$$

where, $W_t$ is the scaffold's weight at a time $t$, $W_d$ is the dry scaffold's weight and $W_e$ is the weight of the swollen scaffolds at the swelling equilibrium at a particular temperature. The weight-swelling ratio ($W/S$) was taken as a parameter to calculate solvent absorption capacity and it is computed as follows: [16]

$$W/S = \frac{(W_e - W_d)}{W_d} \quad (3)$$

### 2.6. Thermal characterization

The thermal properties of the cross-linked gelatin-HA scaffolds were measured using a Q20 Differential Scanning Calorimeter (TA Instruments). The temperature and enthalpy scales were calibrated using standard samples of indium (CAS No.7440-74-6/1, $T_m$ = 156.6 °C, $\Delta H_m$ = 3.295 kJ/mol) and zinc (CAS No.7440-66-6/3, $T_m$ = 419.53 °C, $\Delta H_m$ = 7.103 kJ/mol). The scaffold sample was completely dried by lyophilisation and sealed in a hermetic aluminum pan to prevent any loss of moisture during differential scanning calorimetric (DSC) measurement. The samples had been previously cooled to −20 °C during 1 min. Afterwards they were heated up to 200 °C at a rate 1 °C $min^{-1}$. Upon completing the first heating scan, the sample was quickly cooled at a rate of 10 °C $min^{-1}$ to −25 °C and a rerun of the cooled sample was conducted. Ultrapure nitrogen was used as purge gas at a rate of 20 mL $min^{-1}$ during the measurement. The baseline subtraction was made to correct any heat capacity difference between the sample and the reference furnace. All the experiments were done in triplicate. The specific heat $C_p$ in J $g^{-1}$ $K^{-1}$ of every sample was calculated from the DSC thermogram consisted of heat flow (W $g^{-1}$) by using Eq. (4): [17]

$$C_p = Q' \times 60/r \quad (4)$$

where r is the heating rate of the process in K/min, Q' is heat flow in W $g^{-1}$. The resulting data were used to construct specific heat versus temperature curves.

### 2.7. Compressive strength

The compressive strength of cylindrical samples along the longitudinal and transverse direction was measured with a dynamical mechanical analyzer, MTS Insight electromechanical testing system, using a 1000 N load cell at a strain rate of 0.01 mm $s^{-1}$. We selected a strain rate of 0.01 mm $s^{-1}$ because it is a regular strain rate at which bone is subjected [18] and it is frequently used to test the implantable materials [19]. The compressive strength ($\sigma$) was calculated according to the following formula: [20]

$$\sigma = F/A \quad (5)$$

where $F$ is the applied load (N), and A is the cross-sectional area of the gelatin scaffolds ($m^2$). Ultimate and yield strength, $\sigma_{ult}$ and $\sigma_Y$, as well as compressive modulus, $E$, were obtained from the stress-strain plots [20].

### 2.8. in vitro hydrolytic and enzymatic degradation

Cross-linked gelatin-HA scaffolds were cut into a rectangular shape of about 0.71 cm edges for in vitro degradation studies. The specimens were weighted ($W_0$) and placed in glass test tubes containing 50 mL of PBS (pH 7.4, containing 0.05% w/w of $NaN_3$). Then, these tubes were incubated in a water bath (37 ± 0.1 °C) for 3, 12, 16 and 25 days; PBS was renewed every week. At each time point, samples were collected in triplicate, rinsed thoroughly with distilled water, blotted with filter paper, and oven-dried until constant weight ($W_t$). Assuming that the local pH around the ruffled border of osteoclasts is from 4.0 to 5.0 during bone remodeling period, [21] in vitro degradation under acidic conditions was evaluated by soaking scaffolds in an acetic acid/sodium acetate buffer solution (AcOH buffer) having a pH of 4.24 according to the method of Matsumoto et al. [22] Enzymatic degradation was carried out similarly to the hydrolytic process, including lysozyme (LSZ) into PBS to form an enzymatic degradation medium with a concentration of 4 mg/mL. This concentration was chosen reassembling to the normal LSZ concentrations in plasma that ranges from 4 to 13 mg/mL [23]. The PBS-containing lysozyme was also changed every week during enzyme degradation test. The degradability of cross-linked gelatin-HA scaffolds was estimated from the rate of weight loss ($\%W_L$) accordingly to Tampieri et al.: [24]

$$\%W_L = \frac{(W_0 - W_t)}{W_0} \times 100 \quad (6)$$

### 2.9. Cross-linked gelatin-HA scaffold incubation in simulated body fluid (SBF)

To evaluate the scaffolds bone-bonding potential, the materials were kept in contact with simulated body fluid (SBF) which has a composition and ionic concentration similar to that of human plasma, containing $Na^+$ (142.0 mM), $K^+$ (5.0 mM), $Mg^{2+}$ (1.5 mM), $Ca^{2+}$ (2.5 mM), $Cl^-$ (148.8 mM), $HCO_3^-$ (4.2 mM), $HPO_4^{-2}$ (1.0 mM) and $SO_4^{-2}$ (0.5 mM). Following the standard procedure described by Kokubo et al. [25], the created materials were incubated in a water bath (37 ± 0.1 °C) in 1.5 SBF for periods of 7, 14 and 21 days; the specimens were removed the from fluid, rinsed with distilled water and oven – dried at 40 °C until constant weight.

### 2.10. Statistical analysis

All experiments were conducted at least three times and all values were reported as the mean and standard deviation (SD). Statistical analysis was carried out by the one-way analysis of variance (one-way ANOVA). The statistical difference between two sets of data was considered significant when $p < 0.05$.

## 3. Results and discussion

### 3.1. Mineralized cross-linked gelatin-HA scaffolds

#### 3.1.1. Microstructural, morphological and topological characterization

The success of a scaffold material requires the activation of the appropriate and beneficial responses from the cells with which it is seeded or from the tissue where it is implanted [26]. A critical configuration of pore degree, interconnection, geometry, orientation and sizes is necessary to maintain the proper cell–cell interactions, the cellular density and to provide the correct mass transfer of oxygen, nutrients and waste products [26]. In order to examine if those characteristics can be attained by the GE-HA nano-rods interaction under the selected experimental conditions, transverse and longitudinal sections of the GE-HA lyophilized solutions were taken and analyzed using FE-SEM; results are shown in Fig. 1. Cross and vertical sections of the samples exhibited a nearly analogous highly interconnected macroporous structure, denoting homogeneity between HA nanoparticles and the organic polymer intermingling; Fig. 1a–d. Nano-sized HA particles were uniformly distributed within the pore walls and no aggregates appeared in pores, their presence was confirmed by X-ray diffraction patterns, Fig. SM1. The width of the open interconnected macropores typically ranges between 35 and 288 μm with a mean pore size of 102 ± 25 μm in their smallest dimension, and from 90 − 1300 μm with an average pore size of 300 ± 32.5 μm in the largest one (more details in Figs. SM2 and SM3). The samples dimensions are comparable to those given in literature [26,27] for materials that resulted

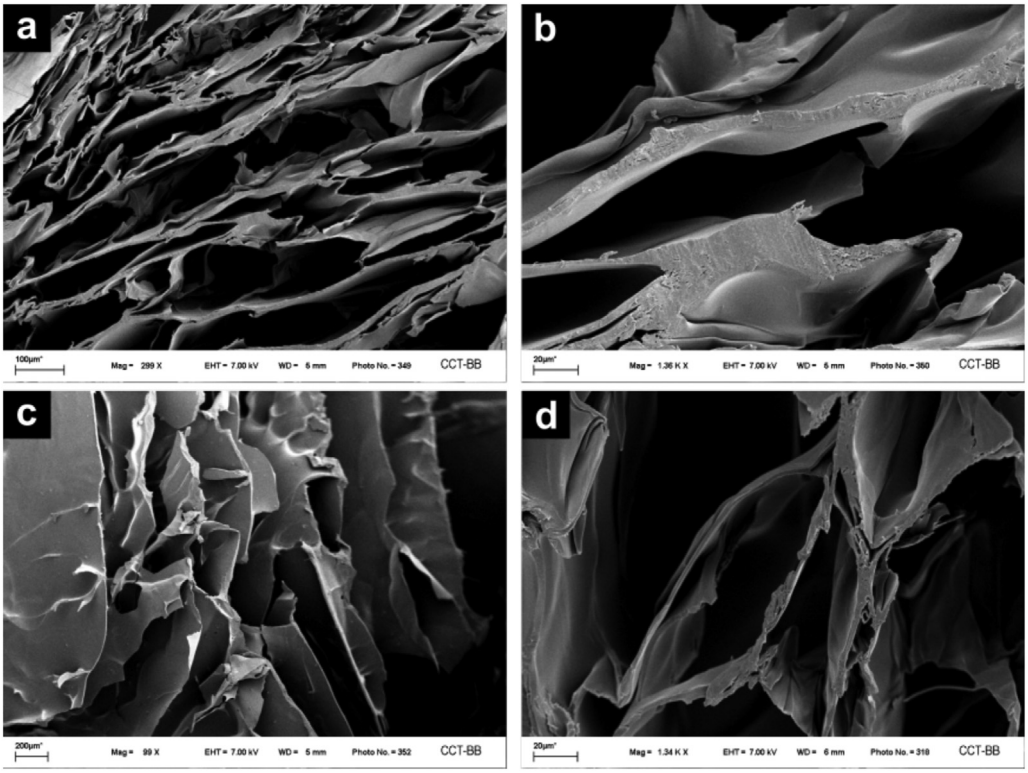


**Fig. 1.** (a–b) Longitudinal and (c–d) transversal FE-SEM microphotographs of lyophilized GE-HA sample, 0.80 g/mL GE and 0.85 mg/mL HA. Scale bars: (a) 100 μm, (c) 200 μm, and (b,d) 20 μm.

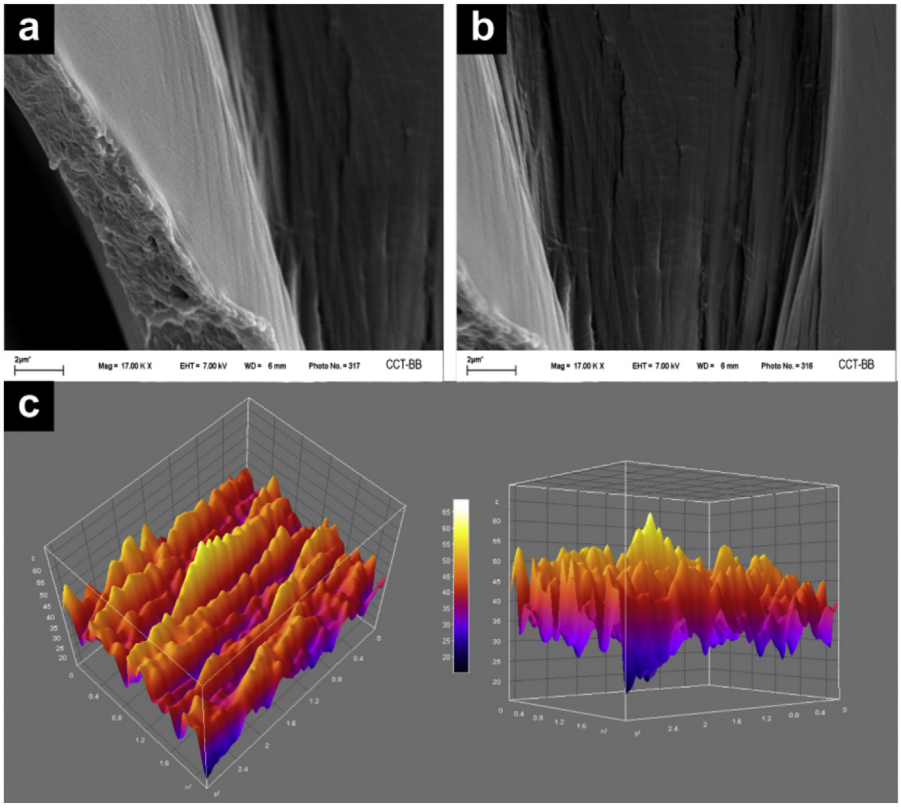


**Fig. 2.** (a,b) Pore wall morphology of lyophilized GE-HA sample, 0.80 g/mL GE and 0.85 mg/mL HA; scale bar: 2 μm. (c) 3D surface profiles of GE-HA scaffolds pore's walls.

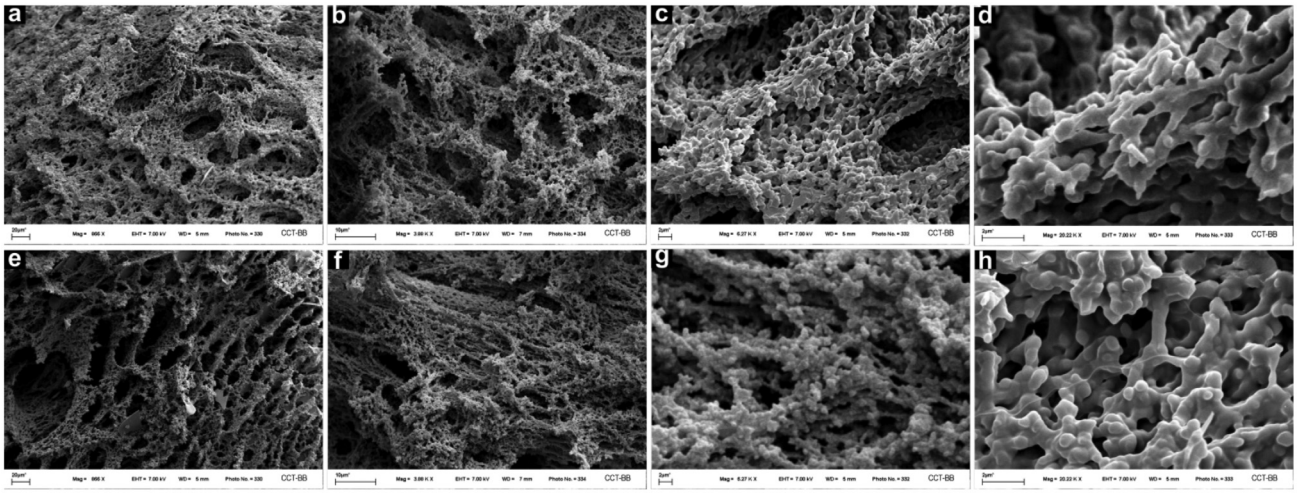


**Fig. 3.** FE-SEM microphotographs of GE-HA-TA cross-linked scaffolds. (a–d) 12.4 mg TA/g GE sample: (a) transversal and (b–d) longitudinal views. (e–h) 33.3 mgTA/g GE sample: (e) transversal and (f–h) longitudinal views. Scale bars: (a,e) 20 μm, (b,f) 10 μm and (c,d,g,h) 2 μm.

in an acceptable cell response, suggesting that it might be suitable for osseous regeneration. The pore wall surface of GE-HA material was not smooth and emerged as an assembly of aligned fibers with more than ten microns in length, Fig. 2a and b. Stress points will arise in the bone adjacent to the implant roughness peaks as a result of the elasticity modulus of the graft material that is substantially higher than that of native tissue [28]. In order to evaluate the pore wall surface roughness and to characterize their asymmetry, surface profiles were performed and Kurtosis ($R_{ku}$) and Skewness ($R_{sw}$) coefficients were computed by means of digitalized scanning electron microscopy (SEM) images, Fig. 2b. The scaffolds' pore walls present positive values of Skewness coefficient ($R_{sk} = 1.592$) showing the presence of a surface profile composed of filled valleys and/or high peaks. The obtained $R_{ku}$ value was of 2.165; since an $R_{ku} < 3$ the distribution curve is said to be platykurtoic and denotes the presence of relatively few high peaks and low valleys, Fig. 2c.

The sharper the asperities of the implant surface roughness, the higher the stress peaks in the bone interface [29] and, excessive bone stresses will result in bone resorption [30]. Taking into consideration that our material exhibits a certain degree of roughness in the pore wall surfaces, but not an excess of high peaks, we suggest that it might lead to less stress and better acceptance by the host tissue. Fig. 3 shows the cross-linked GE-HA scaffolds prepared using two different concentrations of the cross-linked agent (TA); no differences can be appreciated among transversal and longitudinal views. Scaffolds retain their macroporous structure and roughness ($R_{ku} = 2.261$ and $R_{sk} = 1.425$) with a reduction of the mean pore diameter to $72.5 \pm 8.9$ μm, an increased interconnection and valley landscapes on its topography profile. The fiber structure is clearly visible forming a random mesh network and no significant differences can be appreciated on scaffolds' morphology and roughness among the selected TA concentrations.

### 3.1.2. Thermal properties

It is important to carry out studies on the thermal properties of the scaffolds because of changes in thermal stability are good indicators of structuration and cross-linking. Although gelatin is the denatured form of collagen [31]; under the proper conditions, i.e., a scaffolding process activated by a cross-linking agent, the chains are able to undergo into a conformational disorder–order transition and to recover a percentage of the triple-helix structure by a partial renaturation process [31]. The differential scanning calorimetric (DSC) thermograms of the GE-TA and GE-HA-TA scaffolds, shown in Fig. 4, displayed two transitions due to heating. The temperature of the first transition was determined as a point of a sudden increase in the thermogram base line (line *i–ii*), whereas the temperature of the second one was evaluated as the maximum of its endothermic peak (peak *iii*). These temperatures represent the glass ($T_g$) and the melting ($T_m$) transition, respectively. Glass transition seemed to overlap with an enthalpy relaxation phenomena. Several sub-$T_g$ relaxations can be detected in biopolymers [32], as observed in collagenous materials, they could correspond to the intermolecular mobility of tropocollagen molecules (α relaxation mode) and to the intermolecular mobility of polar sequences (β relaxation modes) [33]. These chains' movements are highly sensitive to hydration and the formation of H-bonds; an increment of cross-linking agent concentration or the presence of HA nano-rods provokes the resolution of these transitions and the determination of a sub-$T_g$ temperature, probably due to alterations of the intermolecular bonds and to the rearrangements of gelatin's chains segments linked by these hydrogen bonds. The obtained $T_g$ values were summarized in Table SM2; a higher glass transition temperature respect to uncross-linked gelatin sample can be distinguished with the rise of TA concentration and the incorporation of HA nano-rods indicating an improved thermal stability as a consequence of the increased degree of cross-linking. For the scaffolds prepared

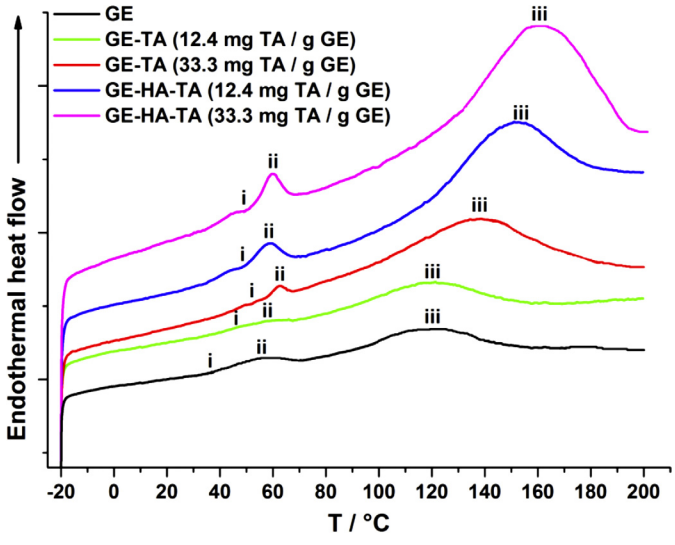


**Fig. 4.** DSC thermograms of GE-TA and GE-HA-TA scaffolds.

with high content of TA and HA nano-rods, DSC thermograms exhibited an endothermic overshoot in the temperature range of the glass to liquid transition. This overshoots are the main signature of enthalpy relaxation during physical aging [34]. They systematically shift to lower temperatures and intensify in magnitude with the presence of HA nano-rods, Table SM2. For the uncross-linked gelatin sample, $T_m$ is referred to as the helix–coil transition [35]. The area underneath the endotherm melting peak divided by the total sample weight ($\Delta H$, J/g) indicates the percentage of structural order in the scaffold. The stability of the helix is primarily dependent on the special features of three polypeptide strands that were held together in a helical conformation by hydrogen bonds, supplemented by inter-chain hydrogen bonds at the positions occupied by glycine [36]. It should be noticed that all the samples used in the DSC analysis were lyophilized exhibiting a negligible water content, which would exclude their potential influence on the denaturation temperature and the enthalpy of helix–coil transition, and hence, the differences in their respective thermal behaviors were a consequence of processing and cross-linking. In all cases cross-linking increases the melting temperature; cross-linked agent plus the presence of HA nano-rods cause a rising of thermal stability in comparison with uncross-linked gelatin sample, Table SM2. The intensification of the transition enthalpy associated with this peak is related to the relative amount of triple helical structure in the samples, and it is significantly greater for the scaffolds containing higher amounts of TA and HA nano-rods. In addition, the superior enthalpy value for the scaffolds prepared with the incorporation of HA nano-rods indicates that it had greater renaturation level than their counterparts, which would result to an improved percentage of elongation values and mechanical strength [37].

The activation energy ($E_a$) values for denaturation of scaffolds are higher than the obtained for uncross-linked gelatin sample, see Table SM2. This clearly shows that more energy is required to denature the scaffolds systems when compared to native gelatin. We turn to consider the heat capacity change due to cross-links, which is much less pronounced than the effect over $T_m$ and the subsequent enthalpy contribution. The results for GE-TA-HA scaffolds with the highest cross-linking agent show a slight $\Delta C_p$ increase as compared with the sample before cross-linking. However, the changes are too small to establish if the cross-links affect the configurational and vibrational contributions of protein stability. Heat capacity can be expressed as the covariance in enthalpy-entropy fluctuations, $C_p = {}^{\delta H \delta S}/_{kT}$, that is an estimation of the entropy-enthalpy compensation [38]. From values of $\Delta H$ and $\Delta C_p$ listed in Table SM2, we can infer that entropy changes are important.

### 3.1.3. Biomimetic mineralization

Mineralized collagen fibers arranged in a complex hierarchical structure are the responsible for bone tissue mechanical properties [2]. Therefore, in addition to a cross-linked structure, it is necessary to replicate the mineralization process of the collagen fibers in bone tissue to provide the synthetic scaffold the correct body-load properties. In general, the mineralization process may be affected by the morphology of the scaffold where the crystals are inserted as well as the presence of nucleation centers that act as growth initiators. In the previous sections it was reported that, although having an influence on the structure and thermal stability of the scaffold, the selected TA concentrations did not affect their morphology and roughness, so its influence in the mineralization process was discarded. Nevertheless, the presence of pre-embedded HA nanoparticles that can act as crystallization nucleation centers could have a clear control on the mineralization's progression. Their impact on the scaffold mineralization will be analyzed below. The recorded SEM images, Fig. SM4, revealed that mineralization occurred in both cross-linked GE scaffolds regardless of nano-HA particles incorporation, and that took place not only on the material surface but also in the pore interior, forming a core-shell GE-mineral structure that bundles and eventually forms a continuous network. The crystal morphology of the deposited layer varies from one sample to another: hexagonal plate-like and needles-like crystals grew on the scaffold not containing nanoparticles (GE-TA), Fig. SM4a–d, while only plate-like shaped crystals of different size are deposited on GE-HA-TA scaffold, Fig. SM4e and SM4f . X-ray diffraction patterns (DRX) indicated that both in GE-TA and GE-HA-TA scaffolds the crystalline phase involved in mineralized matrices resembles to poor crystallized hydroxyapatite, exhibiting a similar peak configuration than the calcium deficient hydroxyapatite (cdHA) present in bone [39], Fig. SM5. Using crystal structure refinement from molecular modeling and Rietveld method [40], detailed information is given in Figs. SM6 and SM7, it can be observed that there is a slight difference between experimental diffraction data and the theoretical data computed for the stoichiometric crystal of hydroxyapatite, Fig. 5a. Consistently, we have obtained a reproduction of a defective HA crystal with a minimal discrepancy with the experimental measurements, Fig. 5b. No peaks suggesting the existence of other calcium phosphate polymorph different than cdHA were detected in the analyzed X-ray diffraction patterns; however the X-ray energy dispersive (EDX) microanalysis shows a Ca/P molar ratio of 1.56 and 1.33 for the mineralized GE-HA-TA and GE-TA scaffolds respectively, detailed information is given in Figs. SM8 and SM9 . The reduced Ca/P molar ratio observed on the mineralized GE-TA scaffold can be associated with the existence of a mixture of cdHA and amorphous calcium phosphate (ACP) phases. ACP possess a chemical formula of $Ca_xH_y(PO_4)_z{\cdot}nH_2O$, n = 3–4.5 with a 5–20 wt% of water content and a variable Ca/P molar ratio of 1.2-2.2 [41]. This polymorph presents an X-ray diffraction pattern without discernible peaks from lattice periodicities [42]. In spite of the apparent similitude of the mineralized scaffolds X-ray diffraction profiles, slight differences can be attained from the analysis of interplanar d-spacing, Fig. SM10, and the computed crystallographic parameters, Table SM3. The d-spacing values position as well as an increment in unit cell volume may vary with partial dehydration in agreement with our previously exposed impression suggesting the presence of ACP in the GE-TA scaffold's mineralized phase.

When the *c/a* ratios of the unit-cell parameters are evaluated, Table SM3, it can be noted that the *c/a* ratio that correspond to the inorganic phase of mineralized GE-HA-TA scaffold (*c/a* = 0.7333) is slightly larger than the *c/a* ratio of hexagonal standard HA (*c/a* = 0.7306) but comparable to the value reported by Smith and Smith [43], and Meneghini et al. [39] for adult bone biogenic apatite (*c/a* = 0.7326). In addition to phase recognition and the resolution of the unit-cell dimensions, XRD can be used to determine the orientation of crystalline facets. The profiles of GE-TA and GE-HA-TA mineralized-sample patterns show signs of strong anisotropy in the peak broadening. From a close inspection of the diffraction profiles reported in Fig. SM5, it is noticeable that the 00l reflections ((001), (002) and (004)) in both samples are sharper than the other reflections of the XRD pattern. The sharper 00l reflections suggest that the coherent diffraction domains preferentially extend along the crystallographic *c* direction, as in biogenic apatite crystals [39]; in fact, there was a 73% of *c*-plane orientation degree ($\Phi$ %) in both mineralized-scaffolds, Table SM3. The extension of crystallographic domains along *c*-axis and lengthwise to the scaffolds mineralized fibrils was confirmed by inspection of mineralized scaffolds by H-TEM, Fig. 6. Selected – area electron diffraction (SAED) patterns extracted from the Fourier transform (FFT) of high resolution TEM images by digitalized image processing analysis confirmed the crystalline nature of cdHA phase and the inter-planar distance of $0.341 \pm 0.041$ nm that corresponds to the (002) crystallographic plane, further analysis is presented in Figs. SM11 and SM12 .

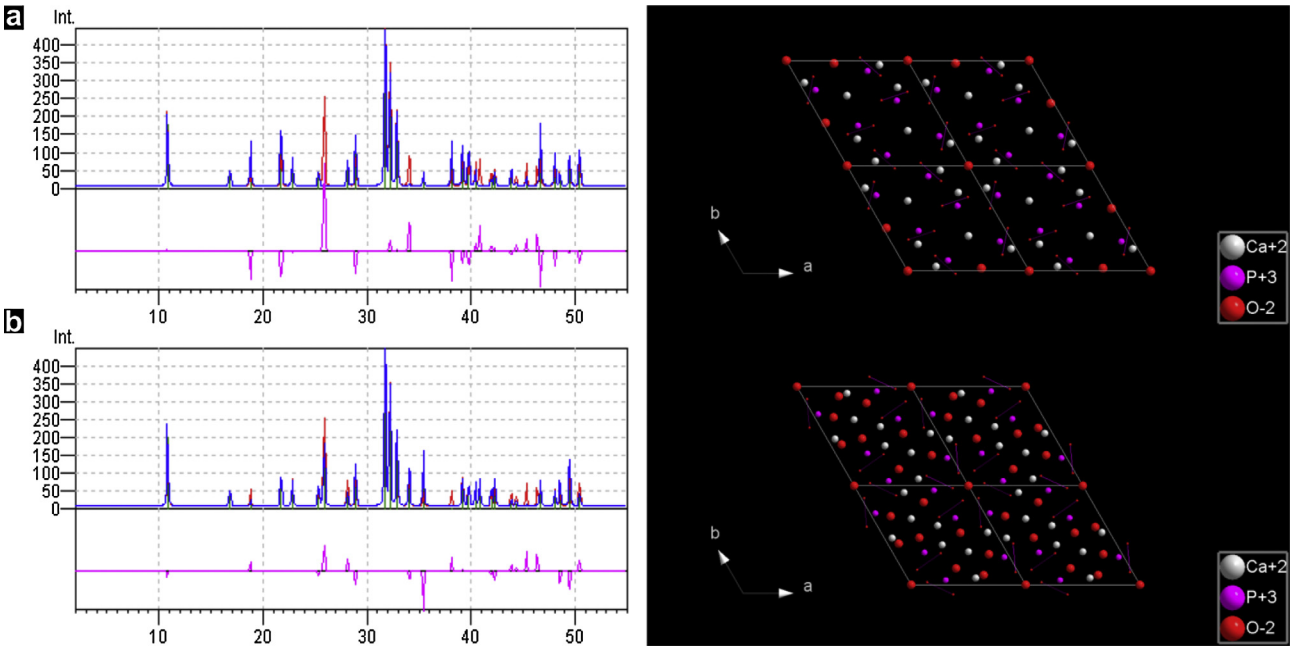


**Fig. 5.** Molecular modeling of (a) stoichiometric and (b) defective crystal of HA. X-ray diffraction patterns: (blue) theoretical data, (red) experimental data and (pink) correlation of theoretical and experimental data, a perfect correlation should be represented by a straight line. (For interpretation of the references to colour in this figure legend, the reader is referred to the web version of this article.)

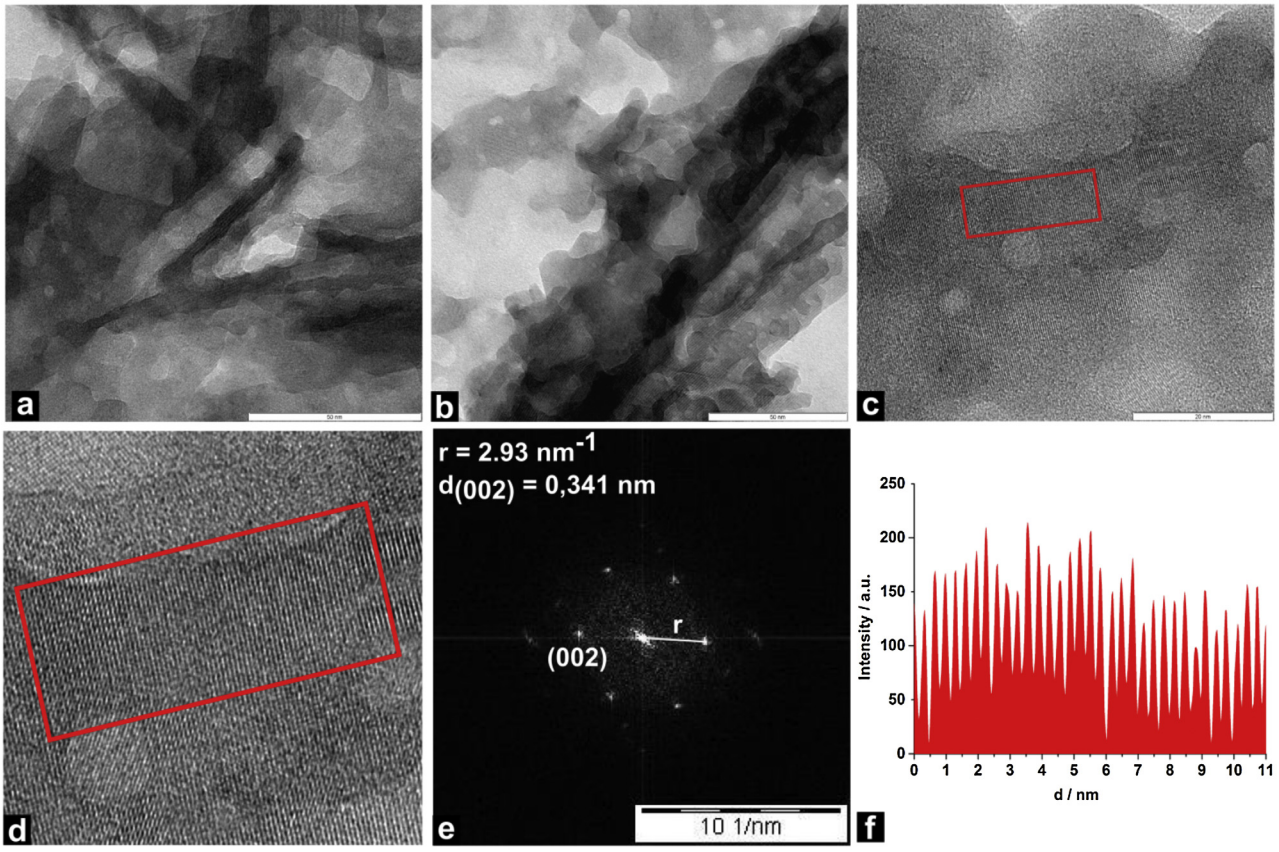


**Fig. 6.** (a–c) H-TEM microphotographs of GE-HA-TA (12.4 mg TA/g GE) mineralized scaffolds; (d, e) selected area electron diffraction analysis (SAED) exhibiting the (002) planes; (f) interlayer distance profile of plane (002). Scale bars (a, b) 50 nm and (c) 20 nm.

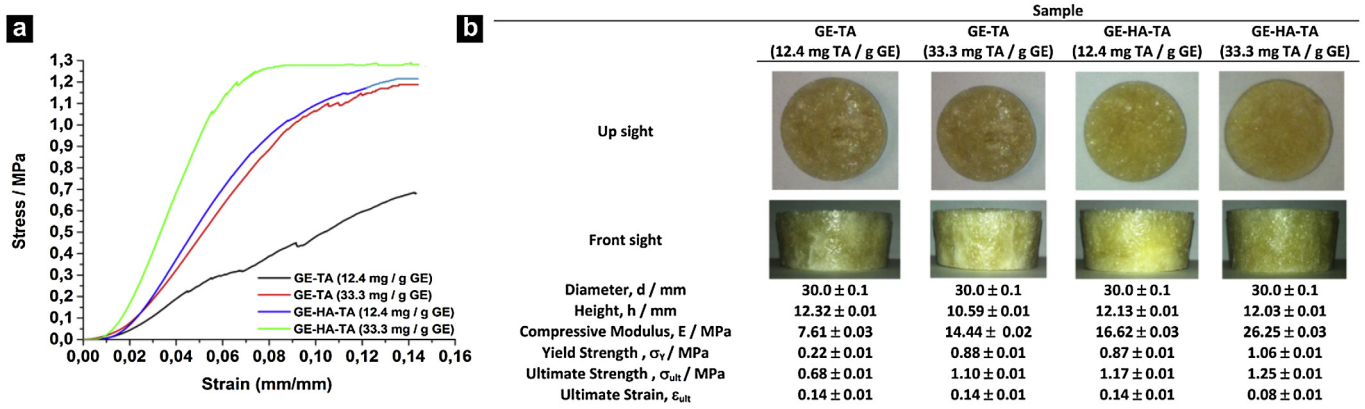


**Fig. 7.** (a) Stress-Strain curves obtained for GE-TA and GE-HA-TA scaffolds; (b) Compression parameters.

The obtained results suggest an intimate relationship between the presences of pre-embedded HA nanoparticles on gelatin scaffolds and the mineralized phase deposition denoting their potential role in the process of bio-mineralization.

### 3.2. Cross-linked gelatin-HA scaffolds as potential platforms for bone tissue engineering

#### 3.2.1. Mechanical against structural attributes

The proportion and circumstances of bone-implant integration have been associated to a requirement on pore size, open porosity volume fraction and interconnectivity, both as a function of structural permeability and mechanics [2]. To determine how the mineralized scaffolds behave mechanically and if their properties are appropriate to avoid collapse during handling and during the patient's normal activities, uniaxial compression tests were performed under controlled environmental conditions. The obtained stress-strain curves are shown in Fig. 7a and the material properties described by both compression modulus and strength data are summarized in Fig. 7b. All materials displays plots that deviate from linearly regarding to plastic deformation, similar than bone tissue [44]. There is an increased stiffness and strength of the scaffold, revealed by the expansion of the compressive modulus and the ultimate and yield strength parameters, by rising the amount of

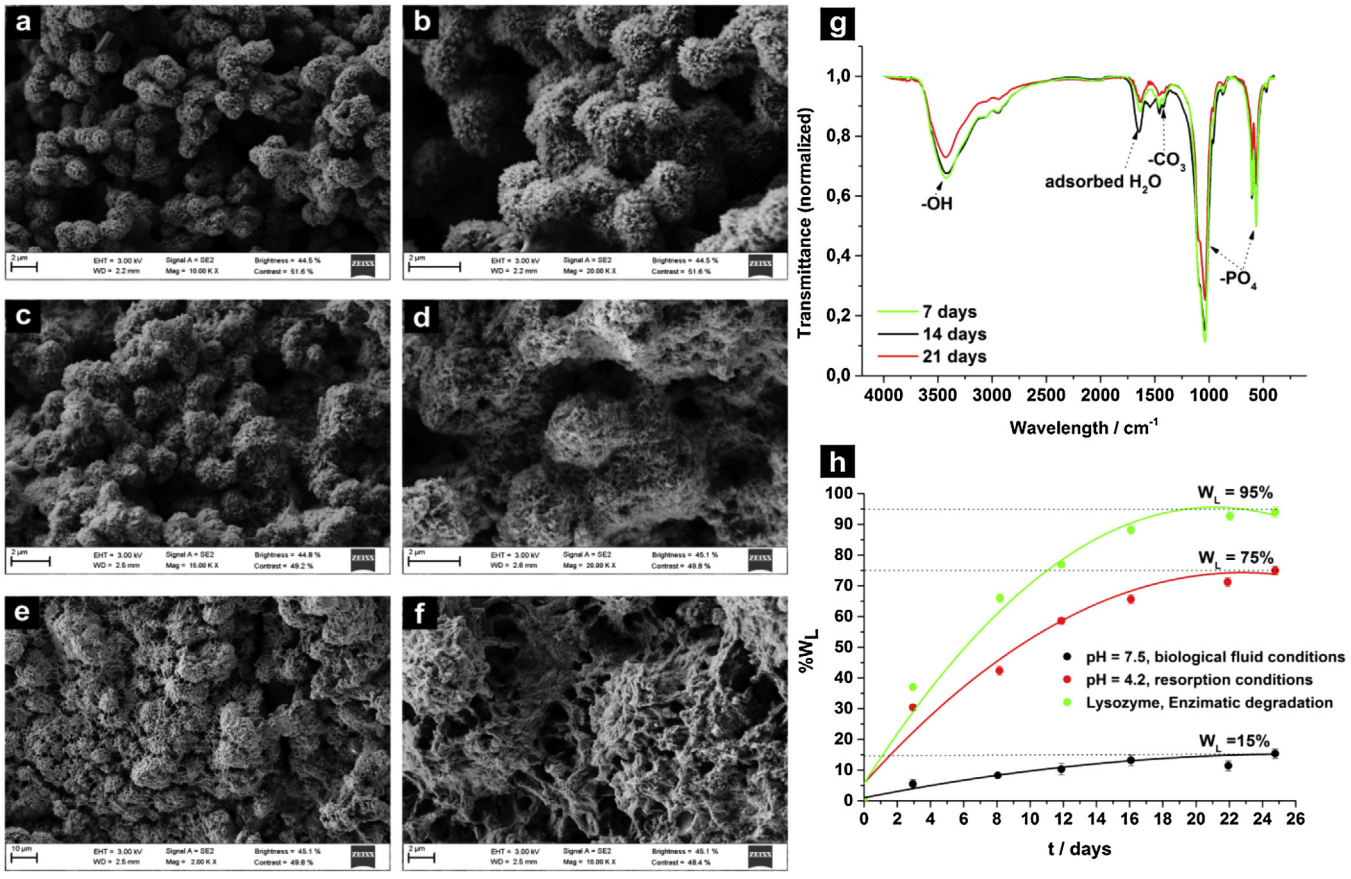


**Fig. 8.** Biomimetic growth of HA crystals after (a–b) 7 days; (c–d) 14 days and (e–f) 21 days of immersion in SBF. (g) FT-IR of GE-HA-TA scaffold after immersion in SBF. (h) GE-HA-TA scaffold kinetic degradation process. Scale bars (a–e) 2 μm and (f) 10 μm.

crosslinking agent and the presence of HA nano-particles. However the combination of high amounts of cross-linked agent to the presence of nanoparticles decreases the scaffold strain capacity. The increase in mechanical properties can be attributed to the ability of HA nano-rods to reinforce the covalently cross-linked GE-TA network and their effect on scaffold mineralization along the polymer network.

As the scaffold was over-cross-linked, as happened with GE-HA-TA (33.3 mg TA/g GE), the gelatin walls became brittle and were easily broken displaying a reduction of the ultimate strain. The compressive *E* values of the obtained scaffolds are comparable to those reported in the literature for healthy cancellous bone [45]. The scaffold open porosity is an important property in tissue engineering, increased open porosity and pore size facilitate bone ingrowth [26,27], however its presence result in a reduction of mechanical properties, since this compromises the structural integrity of the scaffold [16]. All tested scaffolds exhibited an average open porosity volume fraction of about (70 ± 8) % without any significant statistical difference, Fig. SM 13. The open porosity is in accordance with the results derived from SEM analysis. In spite of not exhibiting significant differences in their open porosity, large contrasts among their permeability abilities can be appreciated, Fig. SM13. Highly cross-linked scaffold shows a facilitated entrapment of water in their framework, due to a narrow pore distribution which captures and holds water through capillary action. In addition the swelling behavior of GE-HA-TA scaffolds is superior which may be due to the incorporation of nano-HA particles that contribute to the increase of water uptake because of its water adsorbing properties [46]. From comparing scaffolds prepared with the smallest amount of crosslinking agent (GE-TA and GE-HA-TA containing 12.4 mg TA/g GE), it can be exposed that the high open porosity volume fraction affects the structural integrity of the material and for that reason the scaffold displayed an inferior mechanical strength; nevertheless the presence of nano-HA particles and their effect on the reinforcement of the structure is sufficient to overcome this fact. The effect of HA nano-particles on the scaffold mechanical strength was also noticeable in the material prepared with higher amount of cross-linking agent; however in this case it also provokes a reduction of the ultimate strain.

### *3.2.2. Assessment of bone-bonding potential and in vitro bio-degradability*

On basis of the previous results, the mineralized GE-HA-TA (12.4 mg TA/g GE) scaffold was selected as the specimen with the best mechanical properties, thermal stability, open porosity volume fraction and structural permeability to indirectly evaluate their potential use in bone tissue reparation. In vivo, degradability can be attained by simply dissolution in biological fluids or cell mediated interactions [21,47]. The scaffolds degradability was analyzed in three different situations: (i) dissolution under pH = 7.4 conditions concerning to physiological fluids; (ii) dissolution under pH = 4.2 conditions regarding to resorption process in charge of osteoclast and (iii) dissolution by enzymatic catalyzed decomposition. The results, Fig. 8h, clearly show that the initial degradation rate as well as the scaffold maximum degradation was attained after enzymatic catalyzed conditions, followed by the degradation under resorption conditions (pH = 4.2). The scaffold also experiment a partial degradation (15%) under physiological fluids conditions and that affect the deposition of biogenic HA crystals, Fig. 8a–f, an essential processes to ensure osseo-integration [25].

Bioactivity is defined as the property of materials to develop a direct, adherent and strong bonding with bone tissue. A simpler method to estimate the bone-bonding potential of materials consists of the immersions of this material in simulated body fluid (SBF). According to Kokubo et al. [25], an essential requirement is the formation of a calcium phosphate layer on the material surface, usually called bone-like apatite. This bone-like apatite seems to activate signaling proteins and cells to start the cascade of events that results in bone formation. [48] In others words, in vitro a way to evaluate the in vivo behavior is from the bioactivity test by immersion of the synthetic material into SBF solution [12]. Fig. 8a–e show the SEM microphotographs of apatite coatings deposited on the studied materials after 7, 14 and 21 days incubation in 1.5 SBF. After the first 7 days of immersion a continuous layer of mineral coating, exhibiting a spherulitic micro-morphology, grew on scaffold surfaces, Fig. 8a and b**.** The nuclei were spherical-like globules with 2 μm in diameter composed by agglomerates of plate-like nano-morphology crystals of ∼150 nm length. After 14 days of immersion in 1.5 SBF, the HA crystal coatings exhibited the same basic micro-morphology but with a reduction of resolution; the perfect spherulitic agglomerates of HA crystals that were visible after 7 days, looked elongated and eroded, Fig. 8c and d. Subsequently, completed the 21 days of immersion it can be appreciated gaps between the spherulitic structures, Fig. 8e and f. We assume that it is due to a partial degradation of the scaffold and thereby to a partial destruction of the structure that supports the deposited HA layer. As seen in the FT-IR spectra, there is a reduction of the peaks relating to hydroxyapatite with the rise of immersion, Fig. 8g. EDX microanalysis, Figs. S14–S16, showed that after the bioactivity assay the material with spherulitic-like coating showed a Ca/P = 1.64 that would be ascribed to HA crystals. A reduction of Ca/P ratio can be appreciated with the increment of immersion time, in agreement with the scaffold degradation time evolution. However at all times the Ca-P globules covering the scaffold surface exhibited a Ca/P ratio close to that exists in the trabecular and cortical bone, and their morphology is similar to that considered essential for the development of events involving osteoblasts to attain osseo-integration [25,48].

## 4. Conclusions

We have developed mechanically robust scaffolds, exhibiting a highly interconnected fiber mesh structure, by optimizing the distribution of HA nano-rods within the gelatin-TA network. Samples showed a definite degree of roughness in the pore wall surface, a quality required to attain a suitable host tissue acceptance. The TA cross-linked effect has a little impact on the framework structure and the roughness parameters, while generates a significantly augment of the scaffold thermal stability. In addition, the homogenously distribution of HA nano-rods among TA and protein chains results in a higher GE renaturation level in comparison with uncross-linked GE leading to an improved strength scaffolding. The presence of nano-HA particles, also induce an enhanced scaffold mineralization, achieving a crystal growth of the shape, composition and orientation equivalent to that presented by the mineral phase of calcified tissues. Highly cross-linked scaffold facilitated the entrapment of water in its framework and this fact leads us to believe that they would have promising water retention properties to prevent the loss of body fluid and nutrients. The mineralized GE-HA-TA (12.4 mg TA/g GE) scaffold was selected as the specimen with the best mechanical properties, thermal stability, open porosity volume fraction and structural permeability to indirectly evaluate their potential use in bone tissue repair. Its degradation properties in different biological conditions, and also their capacity to induce, under physiological fluids, a biogenic hydroxyapatite coating, were assessed. These conditions are necessary for its integration into the host tissue, and were met satisfactorily. In a future work, we will test the scaffold abilities to induce the appropriate cellular interactions.

## Acknowledgements

The authors acknowledge Universidad Nacional del Sur (PGI 24/Q064), Concejo Nacional de Investigaciones Científicas y Técnicas de la República Argentina (CONICET, PIP – 11220130100100CO), Fundación Ramón Areces and Xunta de Galicia (AGRUP2015/11). Also they acknowledge Isabelle Nowlan for technical contributions. JS and ANG have doctoral fellowships of CONICET. PVM is an independent researcher of CONICET.

## Appendix A. Supplementary data

Supplementary data associated with this article can be found, in the online version, at http://dx.doi.org/10.1016/j.colsurfb.2016.05.019.

## References

[1] H.W. Kim, J.C. Knowles, H.E. Kim, Porous scaffolds of gelatin–hydroxyapatite nanocomposites obtained by biomimetic approach: characterization and antibiotic drug release, J. Biomed. Mater. Res. Part B 74 (2005) 686–698.
[2] P. Fratzl, H.S. Gupta, P. Roschger, K. Klaushofer, Bone Nanostructure and its Relevance for Mechanical Performance, Disease and Treatment, Nanotechnology, Wiley-VCH Verlag GmbH & Co. KGaA, 2010.
[3] A.R. Amini, C.T. Laurencin, S.P. Nukavarapu, Bone tissue engineering: recent advances and challenges, Crit. Rev. Biomed. Eng. 40 (2012) 363–408.
[4] J. Sartuqui, N. D' Elía, A.N. Gravina, P.V. Messina, Analyzing the hydrodynamic and crowding evolution of aqueous hydroxyapatite-gelatin networks: digging deeper into bone scaffold design variables, Biopolymers 103 (2015) 393–405.
[5] S.-M. Lien, L.-Y. Ko, T.-J. Huang, Effect of crosslinking temperature on compression strength of gelatin scaffold for articular cartilage tissue engineering, Mater. Sci. Eng. C Mater. Biol. Appl. 30 (2010) 631–635.
[6] F. Zhang, C. He, L. Cao, W. Feng, H. Wang, X. Mo, J. Wang, Fabrication of gelatin–hyaluronic acid hybrid scaffolds with tunable porous structures for soft tissue engineering, Int. J. Biol. Macromol. 48 (2011) 474–481.
[7] M.B. Dainiak, I.U. Allan, I.N. Savina, L. Cornelio, E.S. James, S.L. James, S.V. Mikhalovsky, H. Jungvid, I.Y. Galaev, Gelatin–fibrinogen cryogel dermal matrices for wound repair: preparation, optimisation and in vitro study, Biomaterials 31 (2010) 67–76.
[8] S.-J. Ding, M.-Y. Shie, C.-K. Wei, In vitro physicochemical properties, osteogenic activity, and immunocompatibility of calcium silicate–gelatin bone grafts for load-bearing applications, ACS Appl. Mater. Interfaces 3 (2011) 4142–4153.
[9] A. Ovsianikov, A. Deiwick, S. Van Vlierberghe, P. Dubruel, L. Möller, G. Dräger, B. Chichkov, Laser fabrication of three-dimensional CAD scaffolds from photosensitive gelatin for applications in tissue engineering, Biomacromolecules 12 (2011) 851–858.
[10] C.N. Grover, R.E. Cameron, S.M. Best, Investigating the morphological, mechanical and degradation properties of scaffolds comprising collagen, gelatin and elastin for use in soft tissue engineering, J. Mech. Behav. Biomed. Mater. 10 (2012) 62–74.
[11] C. Peña, K. De la Caba, A. Eceiza, R. Ruseckaite, I. Mondragon, Enhancing water repellence and mechanical properties of gelatin films by tannin addition, Bioresour. Technol. 101 (2010) 6836–6842.
[12] N.L. D'Elía, A.N. Gravina, J.M. Ruso, J.A. Laiuppa, G.E. Santillán, P.V. Messina, Manipulating the bioactivity of hydroxyapatite nano-rods structured networks: effects on mineral coating morphology and growth kinetic, Biochim. Biophys. Acta Gen. Subj. 1830 (2013) 5014–5026.
[13] X. Zhang, M.D. Do, P. Casey, A. Sulistio, G.G. Qiao, L. Lundin, P. Lillford, S. Kosaraju, Chemical modification of gelatin by a natural phenolic cross-linker, tannic acid, J. Agric. Food Chem. 58 (2010) 6809–6815.
[14] T. Taguchi, A. Kishida, M. Akashi, Apatite formation on/in hydrogel matrices using an alternate soaking process: II. Effect of swelling ratios of poly(vinyl alcohol) hydrogel matrices on apatite formation, J. Biomater. Sci., Polym. Ed. 10 (1999) 331–339.
[15] C.A. Schneider, W.S. Rasband, K.W. Eliceiri, NIH Image to ImageJ: 25 years of image analysis, Nat. Methods 9 (2012) 671–675.
[16] N. Kathuria, A. Tripathi, K.K. Kar, A. Kumar, Synthesis and characterization of elastic and macroporous chitosan–gelatin cryogels for tissue engineering, Acta Biomater. 5 (2009) 406–418.
[17] G. Kaletunç, Calorimetry in Food Processing: Analysis and Design of Food Systems, John Wiley & Sons, 2009.
[18] U. Hansen, P. Zioupos, R. Simpson, J.D. Currey, D. Hynd, The effect of strain rate on the mechanical properties of human cortical bone, J. Biomech. Eng. 130 (2008) 011011.
[19] G. Ciardelli, P. Gentile, V. Chiono, M. Mattioli-Belmonte, G. Vozzi, N. Barbani, P. Giusti, Enzymatically crosslinked porous composite matrices for bone tissue regeneration, J. Biomed. Mater. Res. Part A 92 (2010) 137–151.
[20] T.M. Keaveny, W.C. Hayes, Mechanical properties of cortical and trabecular bone, Bone 7 (1993) 285–344.
[21] R. Baron, L. Neff, D. Louvard, P.J. Courtoy, Cell-mediated extracellular acidification and bone resorption: evidence for a low pH in resorbing lacunae and localization of a 100-kD lysosomal membrane protein at the osteoclast ruffled border, J. Cell Biol. 101 (1985) 2210–2222.
[22] T. Matsumoto, M. Okazaki, M. Inoue, S. Yamaguchi, T. Kusunose, T. Toyonaga, Y. Hamada, J. Takahashi, Hydroxyapatite particles as a controlled release carrier of protein, Biomaterials 25 (2004) 3807–3812.
[23] V.N. Uversky, A. Fink, Protein Misfolding, Aggregation and Conformational Diseases: Part B: Molecular Mechanisms of Conformational Diseases, Springer Science & Business Media, 2007.
[24] A. Tampieri, M. Iafisco, M. Sandri, S. Panseri, C. Cunha, S. Sprio, E. Savini, M. Uhlarz, T. Herrmannsdörfer, Magnetic bioinspired hybrid nanostructured collagen–hydroxyapatite scaffolds supporting cell proliferation and tuning regenerative process, ACS Appl. Mater. Interfaces 6 (2014) 15697–15707.
[25] T. Kokubo, H. Kushitani, S. Sakka, T. Kisugi, T. Yamamuro, Solutions able to reproduce in vivo surface-structure changes in bioactive glass-ceramic A-W3, J. Biomed. Mat. Res. 24 (1990) 721–734.
[26] J. Velema, D. Kaplan, Biopolymer-based Biomaterials as Scaffolds for Tissue Engineering, Tissue Engineering I, Springer, 2006, pp. 187–238.
[27] P. Sepulveda, A.H. Bressiani, J.C. Bressiani, L. Meseguer, B. König, In vivo evaluation of hydroxyapatite foams, J. Biomed. Mat. Res. 62 (2002) 587–592.
[28] S. Timoshenko, J.N. Goodier, Theory of Elasticity, vol. 5, McGraw-Hill, New York, 1951 (50o).
[29] S. Hansson, M. Werke, The implant thread as a retention element in cortical bone: the effect of thread size and thread profile: a finite element study, J. Biomech. 36 (2003) 1247–1258.
[30] F. Isidor, Loss of osseointegration caused by occlusal load of oral implants. A clinical and radiographic study in monkeys, Clin. Oral Implants Res. 7 (1996) 143–152.
[31] Y. Zhang, J. Venugopal, Z.-M. Huang, C. Lim, S. Ramakrishna, Crosslinking of the electrospun gelatin nanofibers, Polymer 47 (2006) 2911–2917.
[32] Y. Liu, B. Bhandari, W. Zhou, Glass transition and enthalpy relaxation of amorphous food saccharides: a review, J. Agric. Food Chem. 54 (2006) 5701–5717.
[33] B. Nasser, Rehydration mechanisms in collagen as seen by thermally stimulated current, ESJ 9 (2013).
[34] V.M. Boucher, D. Cangialosi, A. Alegría, J. Colmenero, Enthalpy recovery of glassy polymers: dramatic deviations from the extrapolated liquidlike behavior, Macromolecules 44 (2011) 8333–8342.
[35] P. Sobral, A. Habitante, Phase transitions of pigskin gelatin, Food Hydrocolloids 15 (2001) 377–382.
[36] M.D. Shoulders, R.T. Raines, Collagen structure and stability, Annu. Rev. Biochem 78 (2009) 929.
[37] M. Jridi, N. Souissi, A. Mbarek, G. Chadeyron, M. Kammoun, M. Nasri, Comparative study of physico-mechanical and antioxidant properties of edible gelatin films from the skin of cuttlefish, Int. J. Biol. Macromol. 61 (2013) 17–25.
[38] N.V. Prabhu, K.A. Sharp, Heat capacity in proteins, Annu. Rev. Phys. Chem. 56 (2005) 521–548.
[39] C. Meneghini, M.C. Dalconi, S. Nuzzo, S. Mobilio, R.H. Wenk, Rietveld refinement on X-ray diffraction patterns of bioapatite in human fetal bones, Biophys. J. 84 (2003) 2021–2029.
[40] H. Rietveld, A profile refinement method for nuclear and magnetic structures, J. Appl. Crystallogr. 2 (1969) 65–71.
[41] S.V. Dorozhkin, Nanodimensional and nanocrystalline apatites and other calcium orthophosphates in biomedical engineering, biology and medicine, Materials 2 (2009) 1975–2045.
[42] J.C. Elliott, Structure and Chemistry of the Apatites and Other Calcium Orthophosphates, Elsevier, 2016, pp. 2013.
[43] C. Smith, D. Smith, An X-ray diffraction investigation of age-related changes in the crystal structure of bone apatite, Calcif. Tissue Res. 22 (1977) 219–226.
[44] G.K. Smith, Biomechanics pertinent to fracture etiology, reduction, and fixation, in: C.H. Newton, D.M. Nunamaker, C. Lippincott (Eds.), Textbook of Small Animal Orthopaedics, Lippincott, Philadelphia, 1985, pp. 195–230.
[45] K. Rezwan, Q. Chen, J. Blaker, A.R. Boccaccini, Biodegradable and bioactive porous polymer/inorganic composite scaffolds for bone tissue engineering, Biomaterials 27 (2006) 3413–3431.
[46] N.L. D'Elia, C. Mathieu, C.D. Hoemann, J.A. Laiuppa, G.E. Santillan, P.V. Messina, Bone-repair properties of biodegradable hydroxyapatite nano-rod superstructures, Nanoscale 7 (2015) 18751–18762.
[47] X. Zhou, Q. Cai, N. Yan, X. Deng, X. Yang, In vitro hydrolytic and enzymatic degradation of nestlike-patterned electrospun poly (D,L-lactide-*co*-glycolide) scaffolds, J. Biomed. Mater. Res. Part A 95 (2010) 755–765.
[48] P.S. Vanzillotta, M.S. Sader, I.N. Bastos, G. de Almeida Soares, Improvement of in vitro titanium bioactivity by three different surface treatments, Dent. Mater. 22 (2006) 275–282.